The Journal of Chemical Physics

AIP Publishing

RESEARCH ARTICLE | DECEMBER 17 2025

Microwave and terahertz frequencies of O_2 determined with saturated absorption spectroscopy near 763 nm FREE

Special Collection: Yijing Yan Festschrift

Ya-Qi Cheng (程雅淇) ; Zi-Tan Zhang (章紫覃); Yu-Rong Xu (许玉蓉); Cheng-Xun Zuo (左承勋); Yan Tan (谈艳) ; An-Wen Liu (刘安雯) ✉ ; Shui-Ming Hu (胡水明)

Check for updates

J. Chem. Phys. 163, 234310 (2025)
https://doi.org/10.1063/5.0304720

View Online

Export Citation

Articles You May Be Interested In

Simulation of glint reflectance and determination of surface roughness of turbid coastal and inland aquatic waters

AIP Conf. Proc. (February 2017)

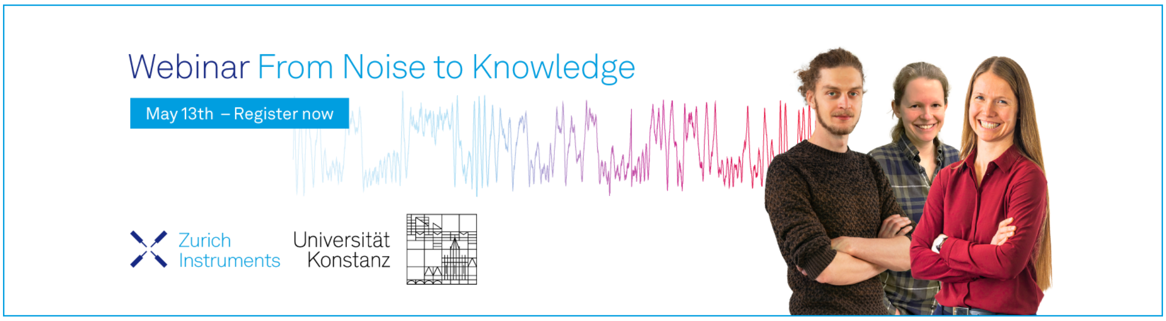

The Journal of Chemical Physics

ARTICLE

pubs.aip.org/aip/jcp

Microwave and terahertz frequencies of O_2 determined with saturated absorption spectroscopy near 763 nm

Cite as: J. Chem. Phys. 163, 234310 (2025); doi: 10.1063/5.0304720
Submitted: 30 September 2025 • Accepted: 2 December 2025 •
Published Online: 17 December 2025

Ya-Qi Cheng (程雅淇),[1] **Zi-Tan Zhang (章紫覃),**[2] **Yu-Rong Xu (许玉蓉),**[1] **Cheng-Xun Zuo (左承勋),**[1]
Yan Tan (谈艳),[2] **An-Wen Liu (刘安雯),**[1,3,a)] **and Shui-Ming Hu (胡水明)**[2,3]

AFFILIATIONS

[1] State Key Laboratory of Chemical Reaction Dynamics, Department of Chemical Physics, University of Science and Technology of China, Hefei 230026, China
[2] Hefei National Research Center for Physical Sciences at the Microscale, University of Science and Technology of China, Hefei 230026, China
[3] Hefei National Laboratory, University of Science and Technology of China, Hefei 230088, China

Note: This paper is part of the Special Topic, Yijing Yan Festschrift.
[a)] **Author to whom correspondence should be addressed:** awliu@ustc.edu.cn

ABSTRACT

We report kilohertz-level precision measurements of magnetic dipole transitions in the $^{16}O_2$ A-band using optical frequency comb-referenced cavity ring-down saturation absorption spectroscopy. Under a zero magnetic field, 30 transitions were recorded with center frequency uncertainties within several kilohertz, representing an improvement of two orders of magnitude over previous studies. From these measurements, 19 $\Delta N = 0$ (microwave) and 12 $\Delta N = 2$ (terahertz) ground-state rotational frequencies were derived using the combination difference method. A global fit of the data produced a new set of spectroscopic parameters for the $X^3\Sigma_g^-(0)$ and $b^1\Sigma_g^+(0)$ states, achieving a root-mean-square deviation of 18 kHz and surpassing earlier benchmarks. Our results reveal systematic deviations in existing terahertz frequency data and demonstrate that saturation spectroscopy provides superior accuracy for determining rotational energies compared to direct microwave or terahertz measurements, particularly at high rotational quantum numbers. This work establishes the most precise frequency reference to date for the oxygen A-band and terahertz region, supporting future advances in high-resolution spectroscopic databases, atmospheric remote sensing, and interstellar O_2 searching.

I. INTRODUCTION

Owing to its stable mixing ratio and homogeneous distribution in Earth's atmosphere, oxygen serves as an excellent tracer for atmospheric remote sensing applications.[1–3] The oxygen A-band, corresponding to the $b^1\Sigma_g^+ \leftarrow X^3\Sigma_g^-$ electronic transition, exhibits the strongest absorption features in the near-infrared to visible spectral region. It offers several distinct advantages, including a broad dynamic range and minimal interference from other atmospheric absorbers, making it a critical window for retrieving key atmospheric parameters. These characteristics have led to the adoption of the oxygen A-band in multiple satellite missions, such as OCO-2/OCO-3,[4–6] GOSAT/GOSAT-2,[7,8] TanSat,[9] and GF-5.[10] These missions enable accurate quantification of the column-averaged dry-air mole fraction of CO_2 (XCO_2),[11–13] cloud properties,[14–16] and aerosol properties.[17,18] Since the first observation of oxygen absorption spectroscopy in 1948, significant improvements have been made in the accuracy of line positions,[19] intensities,[20,21] and line shapes,[22–24] meeting the demands of high-precision remote sensing applications. Notably, the absolute frequencies of eight magnetic-dipole (M1) transitions within the oxygen A-band have been determined with kilohertz-level accuracy,[25] approaching the frequency precision typically achieved in the microwave region.

As the third most abundant element in the universe after hydrogen and helium, oxygen and its chemistry in dense interstellar clouds play a crucial role in characterizing the properties of molecular

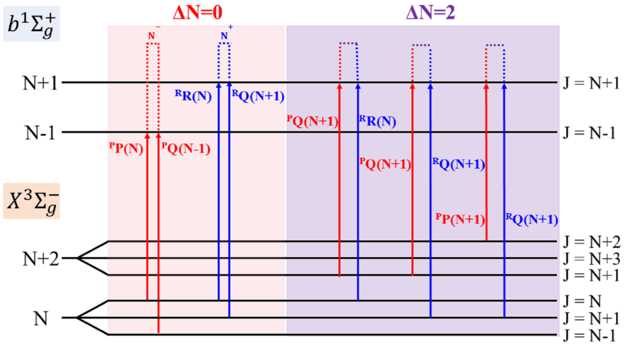

FIG. 1. Diagram of the $b^1\Sigma_g^+ - X^3\Sigma_g^-$ band transitions of O_2.

gas. However, due to strong attenuation by Earth's atmosphere, observations of oxygen transitions near their rest frequencies are not feasible from the ground. Instead, the search for interstellar molecular oxygen has been conducted using orbital observatories such as the *SWAS* (Submillimeter Wave Astronomy Satellite),[26,27] *Odin*,[28] and *Herschel*,[29] primarily through lines at 118.8, 487, 774, and 1121 GHz. Currently, frequency accuracy in the terahertz region remains around 50 kHz.[30,31] This limitation arises because the proportionality between Doppler broadening and transition frequency directly degrades measurement precision by one to two orders of magnitude in the terahertz band compared to the microwave band with the Doppler-limited absorption spectroscopy. Furthermore, improving frequency accuracy with saturated absorption spectroscopy poses a challenge for oxygen pure rotational transitions whose absorption intensities are below 6×10^{-25} cm/molecule.

As illustrated in Fig. 1, certain rovibrational transitions across four sub-branches (^{P}P, ^{P}Q, ^{R}R, and ^{R}Q) of oxygen A-band share common upper energy levels in the $b^1\Sigma_g^+$ electronic state. The frequency differences $\delta\nu$ among these transitions thus yield pure rotational frequencies in the $X^3\Sigma_g^-$ electronic state, spanning both the microwave ($\Delta N = 0$) and terahertz ($\Delta N = 2$) regions.

Complementarily, high-precision infrared saturation absorption spectroscopy offers another pathway for determining ground-state rotational frequencies of molecules. Using the ground-state combination difference method, energy differences between rotational levels in the ground electronic state can be directly deduced. Capable of achieving kHz or even sub-kHz accuracy, this technique enables direct extraction of highly precise lower-state energy levels and spectroscopic parameters—a level of accuracy that may, in some cases, exceed that achievable through direct microwave or terahertz spectroscopy. This approach has been successfully employed for several molecules, such as C_2H_2,[32,33] CO_2,[34,35] and CO,[36] and is particularly advantageous for studying molecular systems that lack dipole-allowed pure rotational transitions.

In this work, we employ optical frequency comb-locked CRDS to perform Doppler-free saturation absorption spectroscopy measurements on the oxygen *A*-band, aiming to acquire transition frequencies with kHz-level accuracy. Based on the experimental results, ground-state rotational energy differences are derived. An effective Hamiltonian model is then used to fit the obtained data. The results not only provide the most precise frequency standards to date for the oxygen *A*-band but also yield accurate microwave and terahertz transition frequencies. These data will support radiative transfer modeling in atmospheric remote sensing and provide references for THz-band observations.

II. EXPERIMENTAL DETAILS

A schematic diagram of the frequency-comb-stabilized cavity ring-down spectrometer is presented in Fig. 2. The setup is similar to that used in our previous work.[25] The light source is a tunable external-cavity diode laser (ECDL, Toptica DL Pro100) operating in the 760–805 nm wavelength range. Its output is split into two beams for "Locking" and "Probing" functions. The "Locking" beam is frequency-shifted by an acoustic-optic modulator (AOM1), phase-modulated by an electro-optical modulator (EOM), and subsequently used to stabilize the laser frequency to a temperature-stabilized, high-finesse optical cavity via the Pound–Drever–Hall (PDH) technique. The "Probing" beam is amplified by a tapered amplifier. This amplified beam is primarily used for CRDS measurements, while a small portion (designated the "Beating" beam)

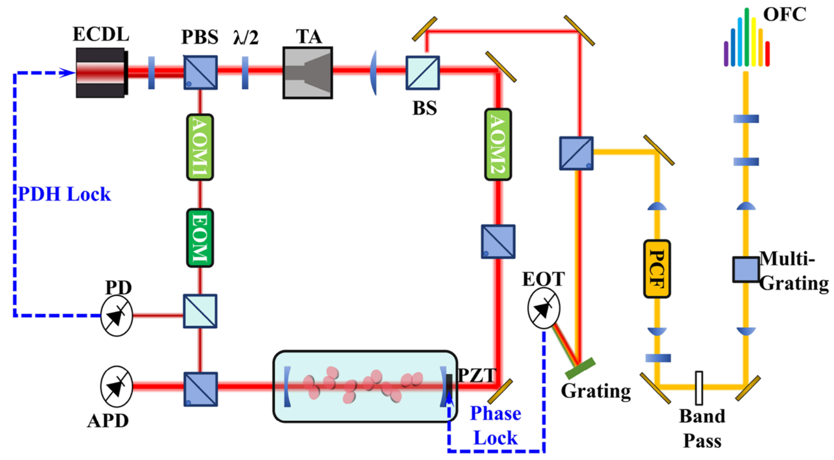

FIG. 2. Configuration of the experimental setup. TA: tapered amplifier; PBS: polarized beam splitter; λ/2: half-wave plate; AOM: acoustic-optic modulator; EOM: electro-optic modulator; PD: photo-detector; APD: avalanche photodiode; and EOT: amplified InGaAs detector.

is diverted for beating with an optical frequency comb to provide precise frequency calibration.

The optical cavity consists of an aluminum spacer holding two high-reflectivity mirrors ($R \sim 99.997\%$ at 760–810 nm, 1 m radius of curvature) separated by 70.3 cm, yielding a free spectral range (FSR) of 213.1 MHz. It is enclosed within a stainless-steel vacuum chamber, which is surrounded by multiple layers of permalloy magnetic shielding to reduce the residual field below 0.05 G. The cavity length is stabilized via a piezoelectric actuator (PZT), controlled by a phase-locked loop that utilizes the beat note between a portion of the "Beating" beam and the optical frequency comb. The frequency comb is generated by frequency-doubling the output of a 1560 nm erbium-doped fiber laser. The fundamental comb is broadened in a photonic crystal fiber to produce a supercontinuum, from which the second harmonic around 780 nm is derived. Both the repetition frequency ($f_{rep} \approx 184.8$ MHz) and the carrier-envelope offset frequency ($f_0 = 20$ MHz) of the comb are phase-locked to a local active hydrogen maser (VCH-1003M).

To minimize optical crosstalk, the "Probing" beam is isolated from the "Locking" beam using a polarizing beam splitter in conjunction with half-wave plates. Before injection into the cavity, the "Probing" beam is frequency-shifted by exactly one FSR using a second acoustic-optic modulator (AOM2) to generate the ring-down signal. The resulting ring-down transient is digitized and fitted to a single-exponential function to extract the ring-down time constant, τ. The absorption coefficient of the sample gas is subsequently calculated as $\alpha = \frac{1}{c\tau} - \frac{1}{c\tau_0}$, where τ_0 is the empty-cavity ring-down time and c is the speed of light. Accordingly, the absolute frequency of the "Probing" beam can be expressed as

$$\nu = 2f_0 + N \times f_r + f_B + f_{AOM2}, \tag{1}$$

where f_{AOM2} represents the frequency shift introduced by AOM2, f_B is the beat frequency between the optical comb and the laser, and N denotes the comb tooth index.

The O_2 gas sample (from Nanjing Tezhong Gas Company), with a purity over 99%, was subjected to "freeze–pump–thaw" purification prior to measurement. Lamb-dip spectra of 30 transitions in the $b^1\Sigma_g^+(0) - X^3\Sigma_g^-(0)$ band were recorded at pressures in the range of 2.0–2.5 Pa.

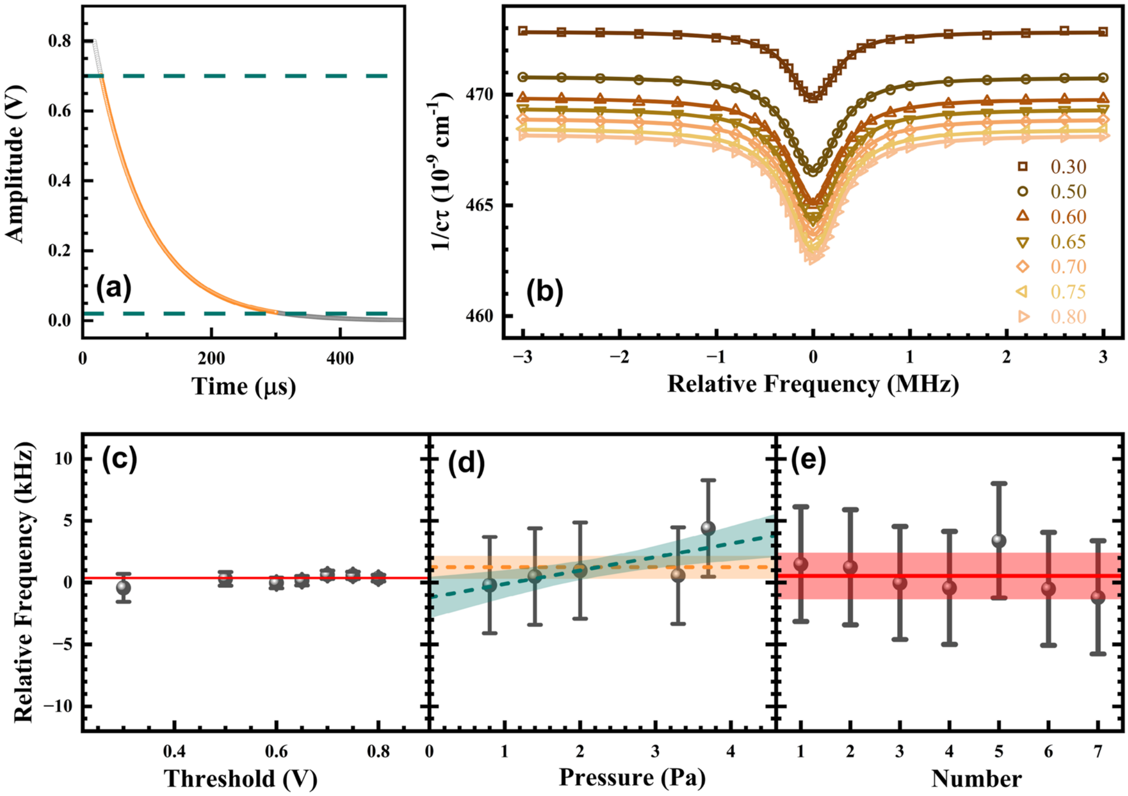

FIG. 3. Position of the $^PQ(6)$ line from saturated absorption spectroscopy. (a) Fitting the ring-down curve between the starting and ending voltages. (b) Saturated absorption spectra of the $^PQ(6)$ line obtained with different starting voltages but the same ending voltage of 0.02 V. (c) Frequencies of the $^PQ(6)$ line obtained with different starting voltages. (d) Frequencies of the $^PQ(6)$ line recorded under different gas pressures. The orange dashed line and the green dashed line represent linear fits without slope and with a free slope, respectively. The shadows represent 1σ confidence regions. (e) Frequencies obtained by seven independent experimental runs over the course of two months. The red line and the shaded area show the mean and its 1-σ uncertainty interval.

III. RESULTS AND DISCUSSIONS

A. Electronic transition frequencies

Figure 3(a) presents the Lamb-dip spectra of the $^{P}Q(6)$ transition under a pressure of 2.1 Pa. The uncertainty budget analysis for the center frequency of this transition is presented in the following, with detailed contributions from individual sources summarized in Table I.

1. Frequency calibration

Owing to the frequency comb being phase-locked to a hydrogen maser, a frequency accuracy of 3×10^{-13} is achieved, corresponding to 0.12 kHz at 760 nm. During spectral measurements, both the signal generator and the frequency counter were referenced to a rubidium clock, with frequency uncertainties below 50 Hz. The overall uncertainty in the frequency calibration is, therefore, less than 0.2 kHz.

2. Locking servo

The signal-to-noise ratio of the beat note between the frequency comb and the laser was ~27 dB, leading to larger frequency fluctuations in the cavity locking servo compared to previous work.[25,37] Based on the Allan deviation of the beat frequency, the corresponding uncertainty is estimated to be ~3.9 kHz.

3. Power shift

The intracavity laser power is estimated to be ~19 W for a 3.0 mW input excitation, based on a combined analysis of the vacuum cavity transmission and the absorption from 2.0 Pa of $^{16}O_2$.[38,39] The AC-Stark shift is negligible at the calculated saturation parameter of $S = 0.1$, which was derived from the saturation power P_s and a full width at half maximum (FWHM) linewidth of 0.5 MHz.

4. Exponential fit range

Fitting the ring-down curves over different voltage regions, as illustrated in Fig. 3(a), has been reported to cause systematic variations.[40] To mitigate this effect, we fitted the ring-down curves using various start voltages (from 0.3 to 0.8 V) while maintaining a fixed end voltage of 0.02 V. This approach led to a noticeable change in the Lamb-dip depths, as shown in Fig. 3(b), while the center frequencies varied by less than 0.1 kHz, well within the experimental uncertainty. As presented in Fig. 1(c), this standard deviation of 0.1 kHz is taken as the estimated uncertainty due to the fitting procedure.

TABLE I. Uncertainty budget of the $^{P}Q(6)$ line position (Unit: kHz). The absolute frequency and its total uncertainty are given in bold.

Source	Frequency	Uncertainty
Statistic	392 752 754 989.6	0.5
Frequency comb		< 0.2
Locking servo		3.9
Pressure shift		2.4
Exponential fit range		0.1
Line profile asymmetry		0.2
Second-order Doppler	+0.34	< 0.1
Total	**392 752 754 990.0**	**4.6**

5. Pressure shift

To determine the corresponding shift in the sub-Doppler regime, Lamb-dip spectra were measured at five sample pressures: 0.8, 1.4, 2.0, 3.3, and 3.7 Pa. The line centers extracted from these spectra are shown in Fig. 3(d). A linear fit yields a slope of 1.2 ± 1.7 kHz/Pa. To evaluate the systematic uncertainty due to the pressure shift, we take the intercept difference of 2.4 kHz between linear fits with the slope fixed at zero and those without constraint. This value is consistent with the pressure shift of 1.2 kHz reported in our previous work on a different transition, $^{P}P(11)$.[25] Moreover, a broader study conducted in the Doppler regime observed shifts ranging from −2.7 to −1.5 kHz/Pa across 26 transitions,[19] which are of the same order of magnitude. Based on this consistency, the pressure-induced shift of 2.4 kHz is adopted as a representative value for the other measured $^{16}O_2$ transitions.

6. Line profile asymmetry

The use of multiple layers of permalloy magnetic shielding effectively suppresses the Zeeman effect. However, residual magnetic fields can still cause slight asymmetries in the spectral line shape. Such distortions appear as systematic residual patterns, with observable asymmetry in the absorption profile. As discussed in previous work,[35,37] this effect is quantifiable and contributes an uncertainty of 0.2 kHz.

7. Second-order Doppler

The second-order Doppler shift is estimated to be −0.34 kHz, calculated using the root-mean-square velocity of 480 m/s for $^{16}O_2$ at 297 K. The associated uncertainty is less than 10 Hz.

8. Statistical and reproducibility

Seven independent experimental runs of the same line were performed over two months, with the results presented in Fig. 3(e). The data points for these runs are plotted with error bars that incorporate all the systematic uncertainties discussed above, along with a statistical error of less than 0.5 kHz. The frequencies agree well with each other, demonstrating excellent reproducibility.

Based on the above, the total uncertainty is 4.6 kHz, and the frequency of the $^{P}Q(6)$ transition is determined to be 392 752 754 990.0 ±4.6 kHz.

For the 29 transitions other than $^{P}Q(6)$, the observed Lamb-dip depths are approximately proportional to the line intensities under comparable intracavity pump laser power, yielding statistical uncertainties ranging from 0.3 to 16.8 kHz. Combined with the systematic uncertainty budget discussed earlier, the total uncertainties for all 30 measured transitions range from 4.6 to 17 kHz. Table II summarizes the measured transition frequencies and their uncertainties, including values for eight transitions previously reported in Ref. 25.

The upper panel in Fig. 4 shows the frequency differences between the HITRAN2020 database[41] and the values measured in this work. Transitions with $\Delta J = \pm 1$ and $\Delta J = 0$ are represented by the orange circles and blue hexagons, respectively, and are labeled with the quantum number m, where $m = -N$ corresponds to $\Delta N = -1$ and $m = N$ to $\Delta N = +1$. The observed deviations range from 0.2 to 0.6 MHz, revealing considerable inaccuracies in the HITRAN database.

TABLE II. Frequencies of the transitions in the A band of $^{16}O_2$ under zero magnetic field, with the unit in kHz. The numbers in parentheses represent 1σ uncertainties in the last quoted digit.

N	^{P}P	^{P}Q	^{R}R	^{R}Q
1			393 519 330 676.8(50)	393 575 595 454.0(28)
3	393 088 346 188.4(47)	393 150 832 444.6(48)	393 672 208 030.6(47)	393 730 654 624.8(47)
5	392 896 509 092.8(46)	392 956 815 147.2(46)	393 813 878 813.5(47)	393 873 469 800.3(46)
7	392 693 590 787.8(46)	392 752 754 991.2(46)	393 944 298 434.1(47)	394 004 733 205.0(47)
9	392 479 602 410.7(18)[a]	392 537 926 288.4(18)[a]	394 063 416 180.5(47)	394 124 566 744.8(46)
11	392 254 548 990.9(33)[a]	392 312 161 477.0(21)[a]	394 171 175 237.4(47)	394 232 975 396.5(47)
13	392 018 429 422.9(31)[a]	392 075 397 631.2(20)[a]		
15	391 771 236 411.2(17)[a]	391 827 599 805.7(15)[a]		
17	391 512 956 495.1(48)	391 568 740 311.6(46)		
19	391 243 569 932.8(58)	391 298 791 323.7(48)		
21	390 963 050 700.4(50)	391 017 721 876.0(88)		
23	390 671 366 407.2(62)	390 725 496 429.7(60)		
25	390 368 478 238(12)	390 422 074 003(10)		
29	389 728 902 414(16)	389 781 444 836(17)		

[a] Frequencies reported by Xu *et al.*[25]

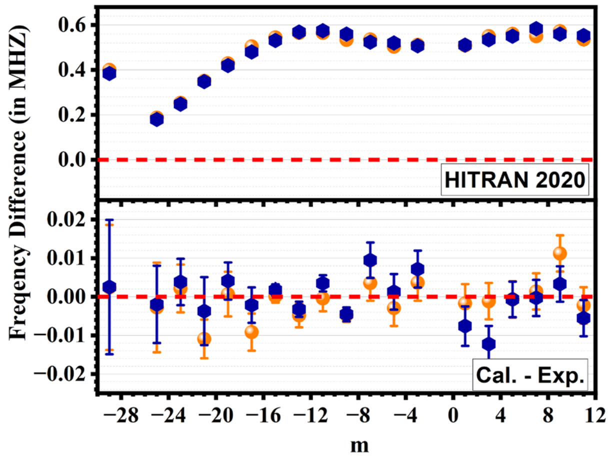

FIG. 4. Upper panel: The frequency differences between those reported in HITRAN2020[41] and those obtained in this work. Lower panel: Differences between the experimental results and those calculated using the spectroscopic parameters obtained in this work (see Table III). The orange balls and the blue hexagons denote transitions of $\Delta J = \pm 1$ and $\Delta J = 0$, respectively.

B. Microwave and terahertz frequencies

As shown in Fig. 1, pure rotational frequencies of oxygen in the microwave ($\Delta N = 0$) and terahertz ($\Delta N = 2$) regions can be directly determined using ground-state combination differences derived from magnetic-dipole transition frequencies in the $b^1\Sigma_g^+(0) - X^3\Sigma_g^-(0)$ band, via the following expressions:

$$\Delta N = 0: \quad \begin{aligned} \nu(\Delta J = -1, N^+) &= \nu_{{}^{R}Q(N+1)} - \nu_{{}^{R}R(N)}, \\ \nu(\Delta J = +1, N^-) &= \nu_{{}^{P}Q(N-1)} - \nu_{{}^{P}P(N)}, \end{aligned} \tag{2}$$

$$\Delta N = 2: \quad \begin{aligned} \nu(\Delta J = +1, N) &= \nu_{{}^{R}R(N)} - \nu_{{}^{P}Q(N+1)}, \\ \nu(\Delta J = 0, N^+) &= \nu_{{}^{R}Q(N+1)} - \nu_{{}^{P}Q(N+1)}, \\ \nu(\Delta J = +1, N^+) &= \nu_{{}^{R}Q(N+1)} - \nu_{{}^{P}P(N+1)}, \end{aligned} \tag{3}$$

where N, N^-, and N^+ indicate that $J = N$, $N - 1$, and $N + 1$ for the lower state, respectively. As a result, we obtained nineteen $\Delta N = 0$ and 12 $\Delta N = 2$ rotational frequencies. These values are compared to previously reported experimental results[31,42] shown in Fig. 5. The literature uncertainties for terahertz transitions[31] range from 14 to 70 kHz—over ten times larger than those in the microwave region (0.3–5.4 kHz).[42] In contrast, the uncertainties from our saturation spectroscopy measurements are ~6.5 kHz for transitions originating from lower states with $N < 21$. Notably, some reported terahertz frequencies deviate from their true values beyond the stated 1σ uncertainty ranges.

C. Rotational parameters in the $V = 0$ states of $b^1\Sigma_g^+$ and $X^3\Sigma_g^-$

The energy levels in the $b^1\Sigma_g^+$ and $X^3\Sigma_g^-$ states can be derived from the following Hamiltonian model:[43]

$$\begin{aligned} \mathbf{H} = {} & T_e + G_v + B_v\mathbf{N}^2 + D_v(\mathbf{N}^2)^2 + H_v(\mathbf{N}^2)^3 \\ & + \frac{2}{3}(3S_z^2 - \mathbf{S}^2)[\lambda_v + \lambda_{D_v}\mathbf{N}^2 + \lambda_{H_v}(\mathbf{N}^2)^2] \\ & + \mathbf{N}\cdot\mathbf{S}[\gamma_v + \gamma_{D_v}\mathbf{N}^2 + \gamma_{H_v}(\mathbf{N}^2)^2], \end{aligned} \tag{4}$$

where T_e is the electronic energy; G_v is the vibrational energy; B_v is the rotational constant; D_v and H_v are the centrifugal distortion constants; λ_v, λ_{Dv}, and λ_{Hv} are the electron spin–spin interaction parameter; and γ_v, γ_{Dv}, and γ_{Hv} are the electron spin–rotation interaction parameters. The rotational levels of the $^3\Sigma_g^+$ electronic state for a given total angular momentum J are obtained by diagonalizing a 3×3 block Hamiltonian containing non-zero matrix elements

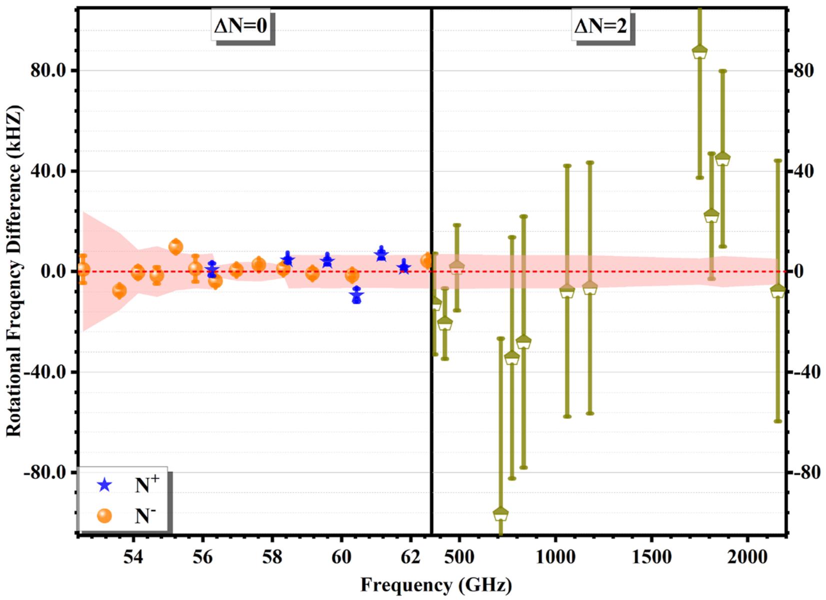

FIG. 5. Comparison of the microwave and terahertz frequencies obtained in this work and those from microwave spectroscopy[42] (left panel) and terahertz spectroscopy[31] (right panel). The red shaded area represents the 1σ uncertainty region determined in this work.

for $\Delta N = \pm 2$, as described in Ref. 44. In contrast, the $b^1\Sigma_g^+$ state has vanishing spin–spin and spin–rotation interactions, and its rotational energy levels can be expressed as a polynomial function of $J(J+1)$.

A total of 101 experimental frequencies, corresponding to 64 rotational transitions from Refs. 31 and 42 together with those combination differences from this work, were utilized to fit a new set of rotational parameters for the $V = 0$ state of $X^3\Sigma_g^-$, which are summarized in Table III. The resulting fit yields a root-mean-square (RMS) deviation of 0.018 MHz, compared to 0.031 MHz reported in Ref. 42. The uncertainties of the present parameters are considerably reduced compared to those previously reported.[42]

Although the differences between the newly determined rotational parameters and those from Ref. 42 lie within reported uncertainties, the rotational energy differences calculated using the two parameter sets increase rapidly with N, reaching 21 MHz at $N = 43$, as shown in Fig. 6(a). It is not possible to determine which parameter set better represents the true energy levels since the $\Delta N = 0$ combination differences—corresponding to rotational transitions in the microwave region—remain below 3 kHz and are thus within experimental uncertainties [Fig. 6(b)]. In contrast, the $\Delta N = 2$ combination differences—associated with terahertz transitions and shown in Fig. 6(c)—display a similar N-dependent trend as in panel (a), reaching up to 8 MHz at $N = 43$. Differences between the two parameter sets are already noticeable at low N values: at $N = 9$, 11, and 13, the deviations approach 20 kHz, several times larger than the experimental uncertainties of this work. Due to the limited tuning range of the laser system used in this work,

TABLE III. Spectroscopic parameters (in MHz) in the $V = 0$ states of $X^3\Sigma_g^-$ and $b^1\Sigma_g^+$.

	$X^3\Sigma_g^- (v = 0)$			$b^1\Sigma_g^+ (v = 0)$	
	This work	Ref. 42		This work	Ref. 19
			T_e	393 387 834.1972(19)	393 387 835.8(3)
B_0	43 100.441 837(19)	43 100.441 83(83)	B_0	41 708.602 121(46)	41 708.6137(3)
$D_0(\times 10^3)$	145.115 37(66)	145.1175(76)	$D_0(\times 10^3)$	160.932 15(30)	160.986(9)
$H_0(\times 10^9)$	20.7(29)	24.9(191)	$H_0(\times 10^9)$	−116.27(69)	−54(6)
λ_0	59 501.343 105(19)	59 501.343 18(25)	$L_0(\times 10^{12})$	−3.38(48)	
$\lambda_D(\times 10^3)$	58.3552(14)	58.3552(21)			
$\lambda_H(\times 10^7)$	3.017(20)	3.017(25)			
γ_0	−252.586 522(17)	−252.586 504(39)			
$\gamma_D(\times 10^6)$	−242.936(92)	−243.018(146)			
$\gamma_H(\times 10^9)$	−1.578(89)	−1.555(111)			
RMS	0.018	0.031	*RMS*	0.0050	0.57
Lines	101	62	*Lines*	38	32

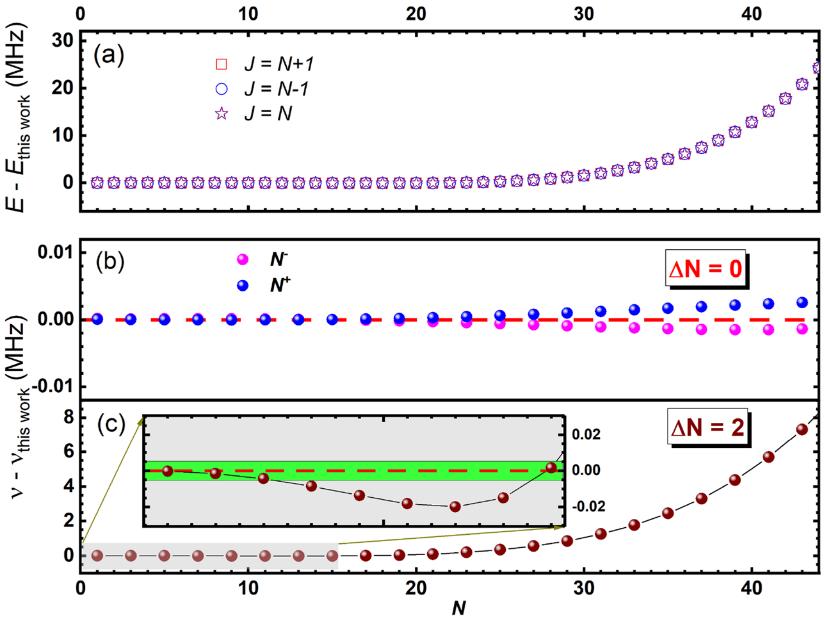

FIG. 6. Difference of results yielded with the parameter from Ref. 42 and those from this work. (a) Rotational energies in the $X^3\Sigma_g^-(0)$ state. (b) Microwave frequencies of the $\Delta N = 0$ lines. (c) Terahertz frequencies of the $\Delta N = 2$ lines. The inset shows results observed in this work, with the green band indicating the experimental uncertainty of $1\sigma = \pm 4.6$ kHz. Note that the energy difference increases rapidly with N. While the differences in $\Delta N = 0$ line positions remain within a few kilohertz, they become substantially more pronounced for $\Delta N = 2$ transitions.

we were unable to observe $\Delta N = 2$ transition pairs with higher N values and thus cannot accurately determine the corresponding energy levels. Nevertheless, the present method clearly demonstrates the feasibility of precisely determining the energy level structure of the $X^3\Sigma_g^-$ ground state. Although direct measurement of $\Delta N = 2$ pure rotational transitions could in principle provide such results, the transition frequencies exceed 2 THz at high N, making high-precision measurements experimentally challenging. Meanwhile, $\Delta N = 0$ microwave spectra are insensitive to the N-dependent energy variations and, therefore, cannot achieve this goal. For convenience, the calculated microwave/terahertz frequencies, the derived energy levels for the X state, and their associated uncertainties are provided in the supplementary material I.

The ground-state rotational parameters and the electronic energy T_e for the $b^1\Sigma_g^+$ state were subsequently determined by fitting 38 transition frequencies using the newly derived rotational parameters of the $X^3\Sigma_g^-(V = 0)$ state. The fit achieves a root-mean-square deviation of 5.0 kHz—an improvement of two orders of magnitude over previous results.[19] A new parameter set can reproduce the observed frequencies within the experimental uncertainties, as illustrated in the lower panel of Fig. 4. The experimental and calculated A-band frequencies, the corresponding energy levels, and their uncertainties are summarized in supplementary material II. Beyond being accurate frequency standards in the 760.4–769.2 nm region, the 38 accurate $^{16}O_2$ magnetic-dipole transitions also permit the study of advanced line profiles involving speed dependence, collisional narrowing, and line mixing-effects key to atmospheric remote sensing.

IV. CONCLUSION

In summary, we have demonstrated kHz-level precision spectroscopy on the magnetically dipole-allowed A-band of $^{16}O_2$ by combining optical frequency comb calibration with cavity ring-down saturated absorption spectroscopy. A total of 30 Doppler-free transitions were measured with kilohertz uncertainties, improving the accuracy of line centers by two orders of magnitude over previous studies. The ground-state combination differences derived from these measurements provided microwave and terahertz rotational frequencies with unprecedented accuracy. These data, combined with existing literature values, enabled a refined determination of the spectroscopic parameters for the $X^3\Sigma_g^-(0)$ and $b^1\Sigma_g^+(0)$ states.

The methodology established in this work highlights the capability of optical comb-referenced saturation spectroscopy in determining ground-state rotational energy levels, particularly for molecules that are challenging to study through direct rotational spectroscopy. For oxygen, this approach overcomes the limitations of both direct THz measurements at high N values and the inherent insensitivity of $\Delta N = 0$ microwave transitions to certain energy-level variations. Our results not only provide the most accurate frequency standards for the oxygen A-band to date but also yield a set of precise rotational energies critical for radiative transfer models. This dataset is expected to serve as a fundamental reference for future high-resolution remote sensing applications, spectroscopic database development, and diverse follow-up studies across multiple disciplines.

SUPPLEMENTARY MATERIAL

See the supplementary material for the experimental and calculated frequencies, and the derived energy levels for the X and b states.

ACKNOWLEDGMENTS

This work was jointly supported by the National Natural Science Foundation of China (Grant Nos. 22273096, 22327801, and 12393825), the Quantum Science and Technology National Major Project (Grant Nos. 2021ZD0303102, 2021ZD0303304, and 2023ZD0301000), and the Chinese Academy of Sciences (Grant No. XDB0970100).

AUTHOR DECLARATIONS

Conflict of Interest

The authors have no conflicts to disclose.

Author Contributions

Ya-Qi Cheng (程雅淇): Data curation (lead); Formal analysis (lead); Investigation (lead); Validation (equal); Writing – original draft (equal); Writing – review & editing (supporting). **Zi-Tan Zhang (章紫覃)**: Data curation (supporting); Investigation (supporting); Methodology (supporting); Writing – review & editing (supporting). **Yu-Rong Xu (许玉蓉)**: Formal analysis (supporting); Investigation (supporting); Methodology (supporting). **Cheng-Xun Zuo (左承勋)**: Formal analysis (supporting); Investigation (equal); Writing – review & editing (supporting). **Yan Tan (谈艳)**: Data curation (equal); Formal analysis (equal); Investigation (supporting); Writing – review & editing (supporting). **An-Wen Liu (刘安雯)**: Conceptualization (equal); Data curation (equal); Funding acquisition (equal); Methodology (equal); Project administration (lead); Supervision (equal); Visualization (equal); Writing – original draft (equal); Writing – review & editing (equal). **Shui-Ming Hu (胡水明)**: Conceptualization (equal); Funding acquisition (equal); Resources (equal); Supervision (equal); Writing – review & editing (equal).

DATA AVAILABILITY

The data that support the findings of this study are available from the corresponding author upon reasonable request.

REFERENCES

[1] M. Choi, S. P. Sander, R. J. D. Spurr, T. J. Pongetti, G. van Harten, B. J. Drouin, D. J. Diner, D. Crisp, A. Eldering, O. V. Kalashnikova, J. H. Jiang, J. J. Hyon, and D. Fu, Remote Sens. Environ. **253**, 112179 (2021).

[2] X. Xu, X. Chen, J. Wang, and L. A. Remer, J. Remote Sens. **4**, 0167 (2024).

[3] N. Xu, Y. Chang, X. Wang, Z. Kong, and L. Mei, Measurement **256**, 118430 (2025).

[4] D. Crisp, H. R. Pollock, R. Rosenberg, L. Chapsky, R. A. M. Lee, F. A. Oyafuso, C. Frankenberg, C. W. O'Dell, C. J. Bruegge, G. B. Doran, A. Eldering, B. M. Fisher, D. Fu, M. R. Gunson, L. Mandrake, G. B. Osterman, F. M. Schwandner, K. Sun, T. E. Taylor, P. O. Wennberg, and D. Wunch, Atmos. Meas. Tech. **10**, 59 (2017).

[5] T. E. Taylor, A. Eldering, A. Merrelli, M. Kiel, P. Somkuti, C. Cheng, R. Rosenberg, B. Fisher, D. Crisp, R. Basilio, M. Bennett, D. Cervantes, A. Chang, L. Dang, C. Frankenberg, V. R. Haemmerle, G. R. Keller, T. Kurosu, J. L. Laughner, R. Lee, Y. Marchetti, R. R. Nelson, C. W. O'Dell, G. Osterman, R. Pavlick, C. Roehl, R. Schneider, G. Spiers, C. To, C. Wells, P. O. Wennberg, A. Yelamanchili, and S. Yu, Remote Sens. Environ. **251**, 112032 (2020).

[6] G. R. Keller, R. A. Rosenberg, A. Merrelli, C. W. O'Dell, G. D. Spiers, V. H. Payne, and A. Chatterjee, IEEE Trans. Geosci. Remote Sens. **63**, 1 (2025).

[7] H. Suto, F. Kataoka, N. Kikuchi, R. O. Knuteson, A. Butz, M. Haun, H. Buijs, K. Shiomi, H. Imai, and A. Kuze, Atmos. Meas. Tech. **14**, 2013 (2021).

[8] R. Imasu, T. Matsunaga, M. Nakajima, Y. Yoshida, K. Shiomi, I. Morino, N. Saitoh, Y. Niwa, Y. Someya, Y. Oishi, M. Hashimoto, H. Noda, K. Hikosaka, O. Uchino, S. Maksyutov, H. Takagi, H. Ishida, T. Y. Nakajima, T. Nakajima, and C. Shi, Prog. Earth Planet. Sci. **10**, 33 (2023).

[9] Y. Liu, J. Wang, L. Yao, X. Chen, Z. Cai, D. Yang, Z. Yin, S. Gu, L. Tian, N. Lu, and D. Lyu, Sci. Bull. **63**, 1200 (2018).

[10] Y. Jiang, X. Wang, H. Ye, H. Shi, Y. Pan, and G. Wang, *International Society for Optics and Photonics* (SPIE, 2023), p. 127060N.

[11] O. Schneising, M. Buchwitz, J. P. Burrows, H. Bovensmann, M. Reuter, J. Notholt, R. Macatangay, and T. Warneke, Atmos. Chem. Phys. **8**, 3827 (2008).

[12] D. Yang, H. Boesch, Y. Liu, P. Somkuti, Z. Cai, X. Chen, A. Di Noia, C. Lin, N. Lu, D. Lyu, R. J. Parker, L. Tian, M. Wang, A. Webb, L. Yao, Z. Yin, Y. Zheng, N. M. Deutscher, D. W. T. Griffith, F. Hase, R. Kivi, I. Morino, J. Notholt, H. Ohyama, D. F. Pollard, K. Shiomi, R. Sussmann, Y. Té, V. A. Velazco, T. Warneke, and D. Wunch, J. Geophys. Res.:Atmos. **125**, e2020JD032794, https://doi.org/10.1029/2020jd032794 (2020).

[13] W. M. Wefers, D. Schmidt, L. W. Lehnert, M. Reuter, M. Buchwitz, C. Kammann, and K. Velten, Atmos. Res. **328**, 108408 (2026).

[14] A. B. Davis, G. Merlin, C. Cornet, L. C. Labonnote, J. Riédi, N. Ferlay, P. Dubuisson, Q. Min, Y. Yang, and A. Marshak, J. Quant. Spectrosc. Radiat. Transfer **216**, 6 (2018).

[15] Y. Lei, S. Li, and J. Yang, Remote Sens. **15**, 3142 (2023).

[16] A. M. Sayer, L. Lelli, B. Cairns, B. van Diedenhoven, A. Ibrahim, K. D. Knobelspiesse, S. Korkin, and P. J. Werdell, Atmos. Meas. Tech. **16**, 969 (2023).

[17] Z.-C. Zeng, S. Chen, V. Natraj, T. Le, F. Xu, A. Merrelli, D. Crisp, S. P. Sander, and Y. L. Yung, Remote Sens. Environ. **236**, 111494 (2020).

[18] Y. Wang, X. Sun, H. Huang, R. Ti, X. Liu, and Y. Fan, Remote Sens. **15**, 948 (2023).

[19] D. J. Robichaud, J. T. Hodges, P. Masłowski, L. Y. Yeung, M. Okumura, C. E. Miller, and L. R. Brown, J. Mol. Spectrosc. **251**, 27 (2008).

[20] D. J. Robichaud, J. T. Hodges, L. R. Brown, D. Lisak, P. Masłowski, L. Y. Yeung, M. Okumura, and C. E. Miller, J. Mol. Spectrosc. **248**, 1 (2008).

[21] E. M. Adkins, S. N. Yurchenko, W. Somogyi, and J. T. Hodges, J. Quant. Spectrosc. Radiat. Transfer **338**, 109412 (2025).

[22] D. A. Long, D. K. Havey, M. Okumura, C. E. Miller, and J. T. Hodges, J. Quant. Spectrosc. Radiat. Transfer **111**, 2021 (2010).

[23] T. Delahaye, X. Landsheere, E. Pangui, F. Huet, J.-M. Hartmann, and H. Tran, J. Quant. Spectrosc. Radiat. Transfer **184**, 316 (2016).

[24] T. M. Petrova, A. M. Solodov, A. A. Solodov, V. M. Deichuli, and A. A. Fedorova, J. Quant. Spectrosc. Radiat. Transfer **314**, 108850 (2024).

[25] Y.-R. Xu, A.-W. Liu, Y. Tan, C.-L. Hu, and S.-M. Hu, Phys. Rev. A **109**, 042809 (2024).

[26] P. F. Goldsmith, D. Li, E. A. Bergin, G. J. Melnick, V. Tolls, J. E. Howe, R. L. Snell, and D. A. Neufeld, Astrophys. J. **576**, 814 (2002).

[27] B. R. Wang, D. Li, P. F. Goldsmith, J. Wu, C. W. Tsai, D. Quan, X. Zhang, J. Wang, G. J. Melnick, J. Z. Li, G. A. Fuller, and J. Xie, Res. Astron. Astrophys. **24**, 095007 (2024).

[28] B. Larsson, R. Liseau, L. Pagani, P. Bergman, P. Bernath, N. Biver, J. H. Black, R. S. Booth, V. Buat, J. Crovisier, C. L. Curry, M. Dahlgren, P. J. Encrenaz, E. Falgarone, P. A. Feldman, M. Fich, H. G. Florén, M. Fredrixon, U. Frisk, G. F. Gahm, M. Gerin, M. Hagström, J. Harju, T. Hasegawa, Å. Hjalmarson, L. E. B. Johansson, K. Justtanont, A. Klotz, E. Kyrölä, S. Kwok, A. Lecacheux, T. Liljeström, E. J. Llewellyn, S. Lundin, G. Mégie, G. F. Mitchell, D. Murtagh, L. H. Nordh, L.-Å. Nyman, M. Olberg, A. O. H. Olofsson, G. Olofsson, H. Olofsson, G. Persson, R. Plume, H. Rickman, I. Ristorcelli, G. Rydbeck, A. A. Sandqvist, F. V. Schéele, G. Serra, S. Torchinsky, N. F. Tothill, K. Volk, T. Wiklind, C. D. Wilson, A. Winnberg, and G. Witt, Astron. Astrophys. **466**, 999 (2007).

[29] P. F. Goldsmith, R. Liseau, T. A. Bell, J. H. Black, J. H. Chen, D. Hollenbach, M. J. Kaufman, D. Li, D. C. Lis, G. Melnick, D. Neufeld, L. Pagani, R. Snell, A. O. Benz, E. Bergin, S. Bruderer, P. Caselli, E. Caux, P. Encrenaz, E. Falgarone, M. Gerin, J. R. Goicoechea, Å. Hjalmarson, B. Larsson, J. Le Bourlot, F. Le Petit, M. De Luca, Z. Nagy, E. Roueff, A. Sandqvist, F. Van Der Tak, E. F. Van Dishoeck, C. Vastel, S. Viti, and U. Yıldız, Astrophys. J. **737**, 96 (2011).

[30] B. A. McGuire, Astrophys. J., Suppl. Ser. **259**, 30 (2022); arXiv:2109.13848.

[31] B. J. Drouin, S. Yu, C. E. Miller, H. S. P. Müller, F. Lewen, S. Brünken, and H. Habara, J. Quant. Spectrosc. Radiat. Transfer **111**, 1167 (2010).

[32] C. S. Edwards, H. S. Margolis, G. P. Barwood, S. N. Lea, P. Gill, and W. R. C. Rowley, Appl. Phys. B **80**, 977 (2005).

[33] A. A. Madej, A. J. Alcock, A. Czajkowski, J. E. Bernard, and S. Chepurov, J. Opt. Soc. Am. B **23**, 2200 (2006).

[34] H. Wu, C.-L. Hu, J. Wang, Y. R. Sun, Y. Tan, A.-W. Liu, and S.-M. Hu, Phys. Chem. Chem. Phys. **22**, 2841 (2020).

[35] Z.-T. Zhang, F.-H. Cao, S. Jiang, A.-W. Liu, Y. Tan, Y. R. Sun, and S.-M. Hu, J. Phys. Chem. A **128**, 2366 (2024).

[36] J. Wang, C.-L. Hu, A.-W. Liu, Y. R. Sun, Y. Tan, and S.-M. Hu, J. Quant. Spectrosc. Radiat. Transfer **270**, 107717 (2021).

[37] J. Wang, Y. R. Sun, L.-G. Tao, A.-W. Liu, and S.-M. Hu, J. Chem. Phys. **147**, 091103 (2017).

[38] G. Giusfredi, S. Bartalini, S. Borri, P. Cancio, I. Galli, D. Mazzotti, and P. De Natale, Phys. Rev. Lett. **104**, 110801 (2010).

[39] L.-S. Ma, J. Ye, P. Dubé, and J. L. Hall, J. Opt. Soc. Am. B **16**, 2255 (1999).

[40] K. Bielska, A. Cygan, M. Konefał, G. Kowzan, M. Zaborowski, D. Charczun, S. Wójtewicz, P. Wcisło, P. Masłowski, R. Ciuryło, and D. Lisak, Opt. Expr. **29**, 39449 (2021).

[41] I. E. Gordon, L. S. Rothman, R. J. Hargreaves, R. Hashemi, E. V. Karlovets, F. M. Skinner, E. K. Conway, C. Hill, R. V. Kochanov, Y. Tan, P. Wcisło, A. A. Finenko, K. Nelson, P. F. Bernath, M. Birk, V. Boudon, A. Campargue, K. V. Chance, A. Coustenis, B. J. Drouin, J. Flaud, R. R. Gamache, J. T. Hodges, D. Jacquemart, E. J. Mlawer, A. V. Nikitin, V. I. Perevalov, M. Rotger, J. Tennyson, G. C. Toon, H. Tran, V. G. Tyuterev, E. M. Adkins, A. Baker, A. Barbe, E. Canè, A. G. Császár, A. Dudaryonok, O. Egorov, A. J. Fleisher, H. Fleurbaey, A. Foltynowicz, T. Furtenbacher, J. J. Harrison, J. Hartmann, V. Horneman, X. Huang, T. Karman, J. Karns, S. Kassi, I. Kleiner, V. Kofman, F. Kwabia–Tchana, N. N. Lavrentieva, T. J. Lee, D. A. Long, A. A. Lukashevskaya, O. M. Lyulin, V. Y. Makhnev, W. Matt, S. T. Massie, M. Melosso, S. N. Mikhailenko, D. Mondelain, H. S. P. Müller, O. V. Naumenko, A. Perrin, O. L. Polyansky, E. Raddaoui, P. L. Raston, Z. D. Reed, M. Rey, C. Richard, R. Tóbiás, I. Sadiek, D. W. Schwenke, E. Starikova, K. Sung, F. Tamassia, S. A. Tashkun, J. Vander Auwera, I. A. Vasilenko, A. A. Vigasin, G. L. Villanueva, B. Vispoel, G. Wagner, A. Yachmenev, and S. N. Yurchenko, J. Quant. Spectrosc. Radiat. Transfer **277**, 107949 (2022).

[42] M. A. Koshelev, G. Y. Golubiatnikov, I. N. Vilkov, and M. Y. Tretyakov, J. Quant. Spectrosc. Radiat. Transfer **278**, 108001 (2022).

[43] S. Yu, C. E. Miller, B. J. Drouin, and H. S. P. Müller, J. Chem. Phys. **137**, 024304 (2012).

[44] R. Larsson, B. Lankhaar, and P. Eriksson, J. Quant. Spectrosc. Radiat. Transfer **224**, 431 (2019).